Hindawi
Journal of Chemistry
Volume 2020, Article ID 3080612, 14 pages
https://doi.org/10.1155/2020/3080612

Research Article

Magnetic Fe_3O_4 Nanoparticle Biochar Derived from Pomelo Peel for Reactive Red 21 Adsorption from Aqueous Solution

Van Hao Nguyen,[1] Huu Tap Van,[2] Van Quang Nguyen,[3] Xuan Van Dam,[3] L. P. Hoang,[4] and L. T. Ha[5,6]

[1]*Faculty of Physic and Technology, TNU-University of Sciences (TNUS), Tan Thinh Ward, Thai Nguyen City, Vietnam*
[2]*Faculty of Natural Resources and Environment, TNU-University of Sciences (TNUS), Tan Thinh Ward, Thai Nguyen City, Vietnam*
[3]*The Center for Technology Incubator and Startup Support, Thai Nguyen University of Agriculture and Forestry, Quyet Thang Ward, Thai Nguyen City, Vietnam*
[4]*Institute of Research and Development, Duy Tan University, Da Nang 550000, Vietnam*
[5]*Ceramics and Biomaterials Research Group, Advanced Institute of Materials Science, Ton Duc Thang University, Ho Chi Minh City, Vietnam*
[6]*Faculty of Applied Sciences, Ton Duc Thang University, Ho Chi Minh City, Vietnam*

Correspondence should be addressed to L. T. Ha; letienha@tdtu.edu.vn

Received 16 March 2020; Accepted 25 May 2020; Published 13 June 2020

Academic Editor: José Morillo

In this study, Fe_3O_4 nanoparticle-loaded biochar derived from the pomelo peel (FO-PPB) was synthesized and applied as an affordable material for the adsorption of Reactive Red 21 (RR21) in an aqueous solution. The characteristics of FO-PPB were evaluated by scanning electron microscopy (SEM), energy dispersive X-ray spectrometry (EDX), X-ray diffraction (XRD), Raman spectra, Fourier transform infrared spectra (FTIR), and Brunauer–Emmett–Teller (BET) surface area. The adsorption process of FO-PPB with RR21 was evaluated through batch experiments to examine various parameters including solution pH, contact time, adsorbent dose, initial RR21 concentration, and solution temperature. Results show that FO-PPB produced by the impregnation ratio between iron (Fe) and pomelo peel biochar (PPB) of 5 : 1 (w/w) had the best adsorption performance. The adsorption capacities of PPB and FO-PPB at optimum experimental conditions (solution pH 3, contact time of 60 min, solution temperature of 40°C, initial RR21 concentration of 300 mg/L, and adsorbent dose of 2 g/L) were 18.59 and 26.25 mg/g, respectively. The adsorption isotherms of RR21 on PPB and FO5-PPB were described well by Langmuir and Sips models with high R^2 values of 0.9826 and 0.9854 for FO5-PPB and 0.9701 and 0.9903 for PPB, respectively. The obtained data also well matched the pseudo-first-order and pseudo-second-order models with R^2 values ≥ 0.96. Chemisorption through sharing or electronic exchange was determined as the main adsorption mechanism.

1. Introduction

Industrial activities such as the production of paint, textile, printing, petrochemical, and cosmetics have positively affected the socioeconomic development. However, the discharge of organic compounds originating from industrial activities greatly contributes to the contamination of the receiving water body [1–7]. The wastewater of textile production has caused a severe pollution due to the toxic characteristics and large volume [8]. Dyes are the main pollutant in the textile wastewater due to its high toxicity and color [9]. Textile industries also cause harm to the environment and human health [10, 11]. Residual dyes in the textile wastewater are difficult to decompose because of its high resistance to light, heat, and oxidizing agents. Reactive Red 21 (RR21) is one of the popular reactive azo dyes that has harmful effects on human health and living organisms [12]. Therefore, RR21 has to be removed as to clean wastewater

before it is discharged into the environment. Many methods such as coagulation, oxidation, biological, and physiochemical methods [13–19] have been developed to remove RR21 as well as other dyes. Nevertheless, low-cost ways to remove RR21 and other dyes from aqueous environments might be developed and applied. Among these techniques, adsorption shows many promises thanks to its easy operation, affordability, and nontoxicity. Activated carbon is a commercial and frequently used adsorbent; however, it is of high cost [14, 20–22]. Recently, biosorbents derived from various kinds of biomass such as green coconut shell, clay, fly ash, sugarcane bagasse, mango kernel, coffee, and rice husk have been applied in many studies regarding the removal of various pollutants from an aqueous solution [23]. Biosorbents have been modified by various methods to enhance the adsorption capacity. Magnetic nanoparticles have emerged as a promising alternative in biosorbent modification because of their large surface area and adsorption efficiency [24, 25]. These adsorbents are also unique, fertile, compatible, easy to synthesize, economical, and environmentally friendly. They can also be easily extracted from mixtures obtained from adsorption processes [26, 27]. However, the main challenge in applying these magnetic nanoparticles is high cost when using these materials alone. This issue can be solved through combining these materials with biochar.

A significant amount of peel waste is generated from pomelo, a popular plant in the Indian Subcontinent and Southeast Asia. Many studies reported that biochar derived from pomelo peel waste could remove organic and inorganic compounds from water and wastewater. Biochar from the pomelo peel with and without modification via H_3PO_4 was applied to discard hexavalent chromium (Cr(VI)) [28], methyl orange dye [29], and Ag and Pb [30] in an aqueous solution. Chen et al. used lanthanum-modified pomelo peel biochar for fluoride removal. Carbamazepine in an aqueous solution was also removed by KOH-modified biochar [31]. Recently, magnetic nanoparticles were used to prepare magnetic biochar. Fe_3O_4 magnetic pomelo peel powder was synthesized for the adsorption of Cu^{2+} [32] and oil-polluted water [33] from an aqueous solution. Iron-doped pomelo peel biochar was applied to adsorb Rhodamine B [34]. However, to the best of the research group's knowledge, no study on using Fe_3O_4 magnetic pomelo peel powder for RR21 removal has been conducted. That is why, this study developed a new adsorbent by modifying pomelo peel biochar and iron nanoparticles derived from Fe_3O_4 to treat Reactive Red 21 from an aqueous solution. The modification of biochar and nanomaterial can enhance adsorption properties. Characteristics regarding structures, morphology, chemical connections, and the surface area were also analyzed accordingly. The results of adsorption isotherms and kinetics were recorded in order to evaluate the performance of the new adsorbent. The effects of pH solution, adsorption time, adsorbent dosage, initial concentrations of RR21, and optimal impregnation ratios of Fe_3O_4 and PPB on adsorption capacity were investigated in detail.

The aim of this study, therefore, was to (i) develop a new adsorbent from synthesizing magnetic Fe_3O_4 nanoparticle pomelo peel biochar and (2) assess the adsorption capacity of Reactive Red 21 (RR21) from an aqueous solutions. Batch adsorption experiments were conducted under several operational conditions (including various impregnation ratios of magnetic Fe_3O_4 nanoparticle pomelo peel biochar, initial pH values, contact times, adsorbent dosages, and initial RR21 concentrations). Moreover, adsorption isotherms and kinetics were also used in order to evaluate adsorption processes.

2. Materials and Methods

2.1. Chemicals. Pomelo peel was collected from a local fruit shop in Thai Nguyen city, Vietnam, before rinsing with tap water two times and with distilled water three times. All chemicals including $FeCl_3.6H_2O$, $FeCl_2.4H_2O$, and ammonia solution (25%) were provided by Merck (Darmstadt, Germany). RR21 (molecular formula $C_{26}H_{19}N_4Na_3O_{15}S_4$) was supplied by Sisco Research Laboratories Pvt. Ltd., Delhi, India. The chemical structure of RR21 is demonstrated in Figure 1.

2.2. Preparing Pomelo Peel Biochar. After washing, the pomelo peel was carbonized at 400°C in an oven (Nabertherm, model L3/11/B170, Germany) under inert gas for 2 h with an increasing heating rate of 5 C/min. It was subsequently cooled, washed with dissolved water, and dried at 105 C to obtain pomelo peel biochar. It was then activated with NaOH (ratio of PPC/NaOH was 3 : 1 w/w) in 24 h. The wet particles were dried again for 2 h at 105 C after undergoing filtration. Finally, the dried solid was activated at 800°C for 3 h under an anaerobic condition to produce activated pomelo peel biochar (PPB).

2.3. Preparation of Magnetic Fe_3O_4 Nanoparticle Pomelo Peel Biochar. Fe_3O_4 magnetic pomelo peel biochar (FO-PPB) was synthesized by the coprecipitation method of ferric, ferrous salts, and PPB with the presence of Ar gas. Firstly, a solution of $FeCl_3{\cdot}6H_2O$, $FeCl_2{\cdot}4H_2O$ (molar proportion: 2 : 1), and PPB in mass ratios of 1 : 1 was added into 150 mL deionized water before being agitated for 45 min. Afterward, 30 mL NH_3 solution (25%) was supplemented into the above solution. Then, the solution was processed by mechanical agitation at 800 rpm under the presence of Ar gas in a flask. The reaction system is kept at 80°C for 60 min, and the solution pH was maintained from 10 to 11 during the process. After the system recovered to ambient condition, the black precipitates were extracted by a permanent magnet and processed with deoxygenated distilled water to neutralize the pH. Finally, the obtained FO-PPB nanoparticles were washed and dried in a vacuum chamber at 60°C for 12 h.

2.4. Characterization. The surface functional groups of PPB and FO5-PPB were determined using a Fourier transform infrared spectroscopy (FT/IR-6300) machine operated at 4000–500 cm^{-1} wavelength. Physicochemical properties of the subject (PPB and FO5-PPB) were identified by an energy

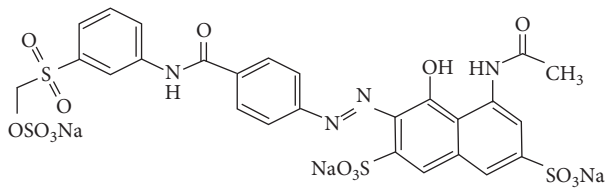

Figure 1: Chemical formula of the RR21 dye.

dispersive X-ray spectroscopy machine (model: Hitachi S-4800) with scanning electron spectroscopy (SEM) and X-ray diffraction pattern (XRD-D8 ADVANCE). Raman spectrum was measured by a Raman spectrometer (at 632.8 nm, Renishaw, UK). Ultraviolet-visible adsorption spectral measurements were carried out by a UV-Vis absorption spectrometer (Jasco-V770, Japan). The BET specific surface areas (S_{BET}) of PPB and FO5-PPB were examined by nitrogen adsorption/desorption isotherms at −196°C (BET, Builder, SSA-4300). The PPB, FO, and FO5-PPB points of zero charge (pH_{PZC}) were clarified using the shift method [35].

2.5. Batch Adsorption Experiments. Adsorption experiments were implemented by the batch method to evaluate the adsorption performance of PPB and FO-PPB against RR21. In a typical experiment, the predetermined amount of FO-PPB was added into 50 mL conical flasks containing 25 mL of RR21 solution. Different experimental parameters, including FO/PPB ratio (1 : 1 ÷ 6 : 1 w/w), initial RR21 concentrations (50–800 mg/L), pH (2–11), contact time (5–120 min), and solution temperature (20–40°C), were investigated to evaluate their effects on RR21 adsorption. The containing flasks were agitated at 120 rpm by a shaker (model: PH-2A, China) at the room condition (25 ± 2°C) and a shaker (model: MaxQ 4000 Benchtop, Thermo Scientific, USA) for temperature control. Sodium hydroxide (0.1 M) and hydrochloric acid (0.1 M) were utilized to control the solution pH. The solutions were then filtered by Whatman No. 1 filter paper with a pore size of 0.22 μm. The residual RR21 in the filtered solutions was analyzed using UV-Vis spectroscopy (Jasco-V770) at an optimal wavelength of 522 nm (corresponding to the maximum adsorption capacity for RR21).

The amount of RR21 adsorbed per mass unit of FO-PPB was calculated using equation (1) to identify the adsorption capacity. The RR21 removal efficiency was determined via the calculations using equation (2):

$$q_e = \frac{(C_o - C_e)V}{m}, \quad (1)$$

$$\mathrm{Re}(\%) = \frac{C_o - C_e}{C_o} \cdot 100\%, \quad (2)$$

where q_e is the amount of dye adsorbed by the adsorbent (mg/g), C_0 is the initial RR21 concentration (mg/L), C_e is the residual RR21 concentration after adsorption (mg/L), m is the mass of the FO5-PPB adsorbent (g), and V is the volume of the RR21 solution (L).

3. Results and Discussion

3.1. Characteristics of Adsorbents. The surface structure is one of the properties that are influential on the adsorption capacity of PPB and FO5-PPB materials. Figure 2 shows the N_2 adsorption-desorption isotherms of N_2 at −196°C of PPB and FO5-PPB. The results indicated that at low relative pressures, the adsorption isothermal increased relatively than at relatively high pressures. This suggests that the main adsorption occurs at relatively low pressures and indicates that the material is highly porous with a narrow size distribution [36]. The specific surface area and total pore volume of PPB obtained were, respectively, 889.8 m^2/g and 0.378 cm^3/g, while FO5-PPB denatured by Fe_3O_4 has a larger surface area and total pore volume, 1061.3 m^2/g and 0.413 cm^3/g, respectively. These results illustrate that with a large surface area and porosity, PPB offers a considerable capacity of contaminant adsorption, while after modified with Fe_3O_4, the presence of Fe_3O_4 between layers of PPB increases the heterogeneity of the adsorbent, resulting in a higher porosity [37]. Consequently, the adsorption capacity of modified materials is enhanced. This result was further illustrated by the SEM images and EDX spectra. SEM/EDX images of PPB, Fe_3O_4 nanoparticles, and FO5-PPB (before and after adsorption) are presented in Figure 3. These results illustrate that PPB had a porous structure (Figure 3(a)) with a smooth surface. In contrast, the surface of Fe_3O_4 nanoparticles (Figure 3(b)) was rough and coarse because the spherical-shaped particles of particle size less than 20 nm were agglomerated and stuck to each other. The SEM micrographs of FO5-PPB (throughout the adsorption process) are shown in Figures 3(e) and 3(f). It can be seen that the distribution of Fe_3O_4 nanoparticles on the surface of PPB is relatively uniform. The surface of the FO5-PPB became more smooth and shiny after adsorbing RR21 (Figure 3(f)).

The EDX spectrum indicates the presence of carbon (C) and oxygen (O) on the PPB structure with the atomic C and O ratio of 74.01 and 25.99%, respectively (Figure 3(c)). Similarly, the O and iron (Fe) ratio (ratio of 61.57 and 38.43%, respectively) was the primary element in the Fe_3O_4 structure (Figure 3(d)). Also, the analysis of EDX (Figures 3(g) and 3(h)) indicates a decrease in the amount of C and the presence of Fe in FO5-PPB in comparison with the pristine PPB and Fe_3O_4 nanoparticles (Figures 3(c) and 3(d)).

In order to study the crystal phase of iron oxide particles, the selected samples were analyzed by powder X-ray diffraction (XRD) operated in 2θ in a range of 15–70°C at 25°C via using Cu kα radiation (λ = 1.54 Å). Figure 4(a) shows the XRD patterns of PPB, Fe_3O_4 nanoparticles, and FO5-PPB (throughout the adsorption process). The XRD analysis results of PPB in Figure 4(a) show the very broad diffraction peaks at the angle of $2\theta \sim 24.04^\circ$ and ~44.7° for PPB, corresponding to the diffraction of (002) and (101) planes, which can be attributed to the characteristic reflection of the amorphous structure [38]. Six diffraction peaks for Fe_3O_4 at the angle of 2θ~30.2°, 35.55°, 43.13°, 53.6°, 57.16°, and 62.78° corresponding to (220), (311), (400), (422), (511), and (440) planes were observed for both Fe_3O_4 and FO5-PPB patterns.

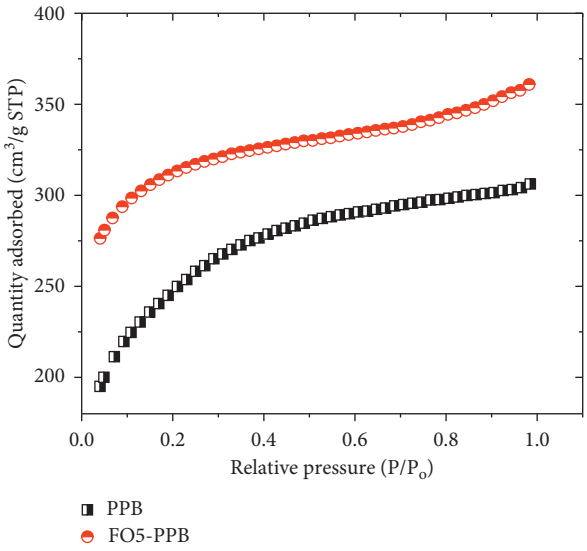

Figure 2: Adsorption isotherms of N_2 at −196°C of PPB and FO5-PPB.

All of these diffraction peaks of Fe_3O_4 were relatively homogenous with the standard Fe_3O_4 diffraction data (JCPDS, Card No. 19-0629) [39–41]. This also illustrates the success in composing Fe_3O_4 and PPB.

Figure 4(b) presents the recorded FTIR spectrum of PPB, Fe_3O_4 nanoparticles, and FO5-PPB (before and after adsorption). In all materials, O–H stretch bonded groups were present at a peak of 3416 cm^{-1}. The results of Hu et al. [42] reported a similar result that the presence of O–H groups was recorded at a peak of 3417 cm^{-1}. Peaks at 2922 cm^{-1} and 2854 cm^{-1} of PPB and FO5-PPB show the C–H stretching vibration [43]. Results that are almost identical have been documented elsewhere in [9]. The peaks at 2358 cm^{-1} and 2337 cm^{-1} in all materials are corresponding to the stretching vibration of the –C=C group [44], while peaks at 1686 cm^{-1} and 1620 cm^{-1} suggested the vibration of the C=O group [45, 46]. Peaks at 1051 cm^{-1} and 1028 cm^{-1} of PPB and FO5-PPB suggested the C–C stretching vibrations [47–50]. The characteristic bands at 582 cm^{-1} of FO and FO5-PPB illustrated the Fe–O stretching vibrations [51]. This is another proof of the success of Fe_3O_4 bonding to the FO5-PPB surface.

The adsorption region at the characteristic wavenumbers for Fe–O and OH bonds shows a slight change of the adsorption peaks of Fe3O4 (~582 cm^{-1}1 and ~3397 cm^{-1}) compared to that of the FO5-PPB sample (~585 cm^{-1} and 3431 cm^{-1}). This can be explained by the interaction between Fe ions (from Fe_3O_4) and the oxygen groups of PPB, affecting the binding state of ferromagnetic particles. The results of FTIR analysis are important evidence for the interaction between ferromagnetic particles and PPB in the formation of FO5-PPB.

In order to determine more details of the vibrational modes and to confirm the composite formation between Fe_3O_4 and PPB, Raman spectra was measured at an excitation wavelength of 635 nm using a Renishaw spectrometer. Figure 4(c) shows Raman spectra of PPB, Fe_3O_4 nanoparticles, and FO5-PPB before and after adsorption. The Raman spectra of PPB displayed two peaks positioned at 1343 and 1575 cm^{-1} that can be denoted, respectively, as D and G bands (Figure 4(c)-A). Out of which, the D band (E_{2g} mode) represents the relative vibration of the atoms that is perpendicular to the aromatic layers (disorder band), whereas, the G band (graphite band) (E_{2g} mode) is the indication of the stretching vibration in the aromatic layers [52–55]. The peaks at 218, 276, and 394 cm^{-1} correspond to the E_g mode, the peak at 485 cm^{-1} corresponds to the T_{2g} mode, and the peak at 594 cm^{-1} corresponds to the A_{1g} mode (Figure 4(c)-B) of iron oxide [56, 57], while the peak at 1298 cm^{-1} corresponds to the second-order scattering of iron oxide.

The two Raman spectra of the synthetic FO5-PPB in the adsorption process of RR21 are presented in Figures 4(c)-C and -D, respectively. The whole spectra displayed almost all the peaks that are characteristic to the Fe_3O_4 magnetite structure and graphite of carbon materials. Peaks at lower Raman shift values (218, 276, 393, 687, and 698 cm^{-1}) (in Figure 4(c)-C and -D) may indicate the vibration modes of Fe–O bonds within each Fe_3O_4 nanoparticle and the Fe–C bonds on the surface of the PPB [58, 59]. The small shifting of some vibration peaks of Fe_3O_4 and D and G bands of PPB in the Raman spectrum of FO5-PPB (Figure 4(c)-C) strongly suggests the good incorporation of Fe_3O_4 nanoparticles into PPB. The influence of adsorbing RR21 was recognized by the shifts of some peaks. In fact, the main peak at around 485 cm^{-1} was recorded via the spectra of the synthesized magnetite before being assigned to the T_{2g} vibrational mode. There was also a peak which appeared at around 687 cm^{-1} in examining spectra (Figure 4(c)-C) and was then classified to be the A_{1g} mode, which is a typical property of the magnetite structure [60]. However, for FO5-PPB after adsorption (Figure 4(c)-D), this peak altered from 687 cm^{-1} to 698 cm^{-1} while the D peak changed from 1361 cm^{-1} to 1379 cm^{-1} and the G peak slightly increased from 1584 cm^{-1} to 1590 cm^{-1}.

3.2. Reactive Red 21 Adsorption

3.2.1. Effect of Impregnation Ratio of Fe_3O_4/PPB on RR21 Adsorption. The necessary experiments were carried out to compare the adsorption efficiency of PPB and six FO-PPBs produced at 6 different ratios (w/w) between Fe ions ($Fe^{3+} + Fe^{2+}$) and PPB, namely, FO1-PPB, FO2-PPB, FO3-PPB, FO4-PPB, FO5-PPB, and FO6-PPB, corresponding to ratios of 1 : 1, 2 : 1, 3 : 1, 4 : 1, 5 : 1, and 6 : 1, respectively. All experiments were set at an initial RR21 concentration of 50 mg/L, solution pH of 3, and ambient temperature (25 ± 2°C). The obtained results are illustrated in Figure 5.

Results from Figure 5 show that the adsorption capacity of RR21 increased significantly corresponded by an increase in the Fe/PPB ratio from 1 : 1 to 4 : 1. It increased slightly when the ratio was 5 : 1 and 6 : 1. The maximum adsorption capacity of RR21 was 24.79 mg/g at the Fe/PPB ratio of 5 : 1. The new adsorbent generated by combining Fe and PPB has much higher adsorption capacity than that of pristine PPB. The presence of Fe on FO-PPB could be the main cause of

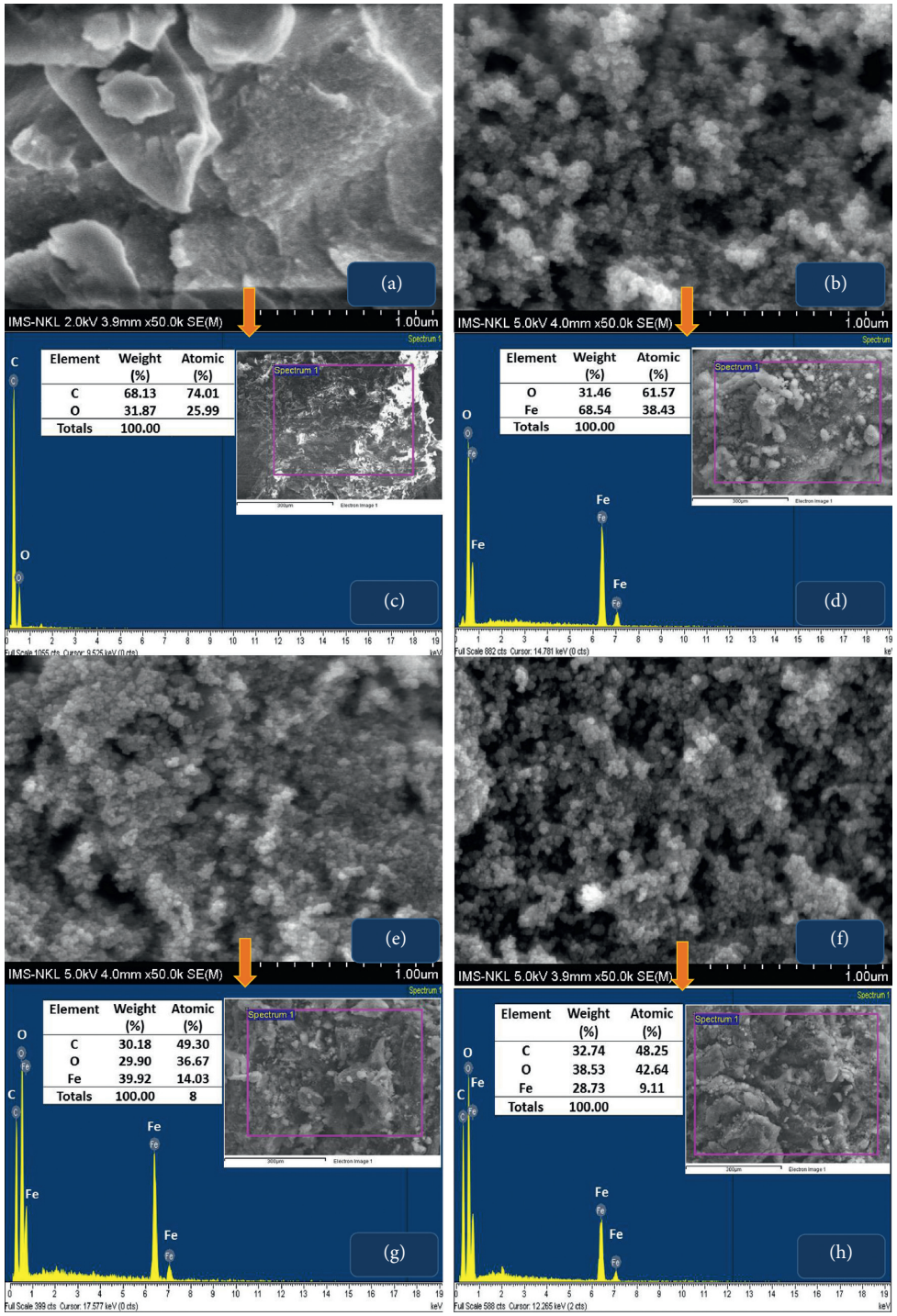

Figure 3: SEM and EDX spectra of PPB (a, c), Fe_3O_4 nanoparticles (b, d), FO5-PPB before adsorption (e, g), and after adsorption (f, h).

this enhancement. The adsorption capacity was almost unchanged when the impregnation ratio was increased from 5 : 1 to 6 : 1. From these results, the suitable impregnation ratio for generation of FO-PPB was 5 : 1 (w/w). Therefore, this impregnation ratio of 5 : 1 for producing Fe_3O_4 magnetic pomelo peel biochar (FO5-PPB) was used for further experiments.

3.2.2. Effect of Initial pH. Solution pH was one of the factors that had an influence on the adsorption process due to its impacts on the surface charge and solubility of the adsorbent [61]. Required experiments were conditioned at various solution pH from 3 to 11 to determine the effects of various solution pH on RR21 adsorption by PPB and FO5-PPB. The results show that the adsorption capacity of RR21 decreased

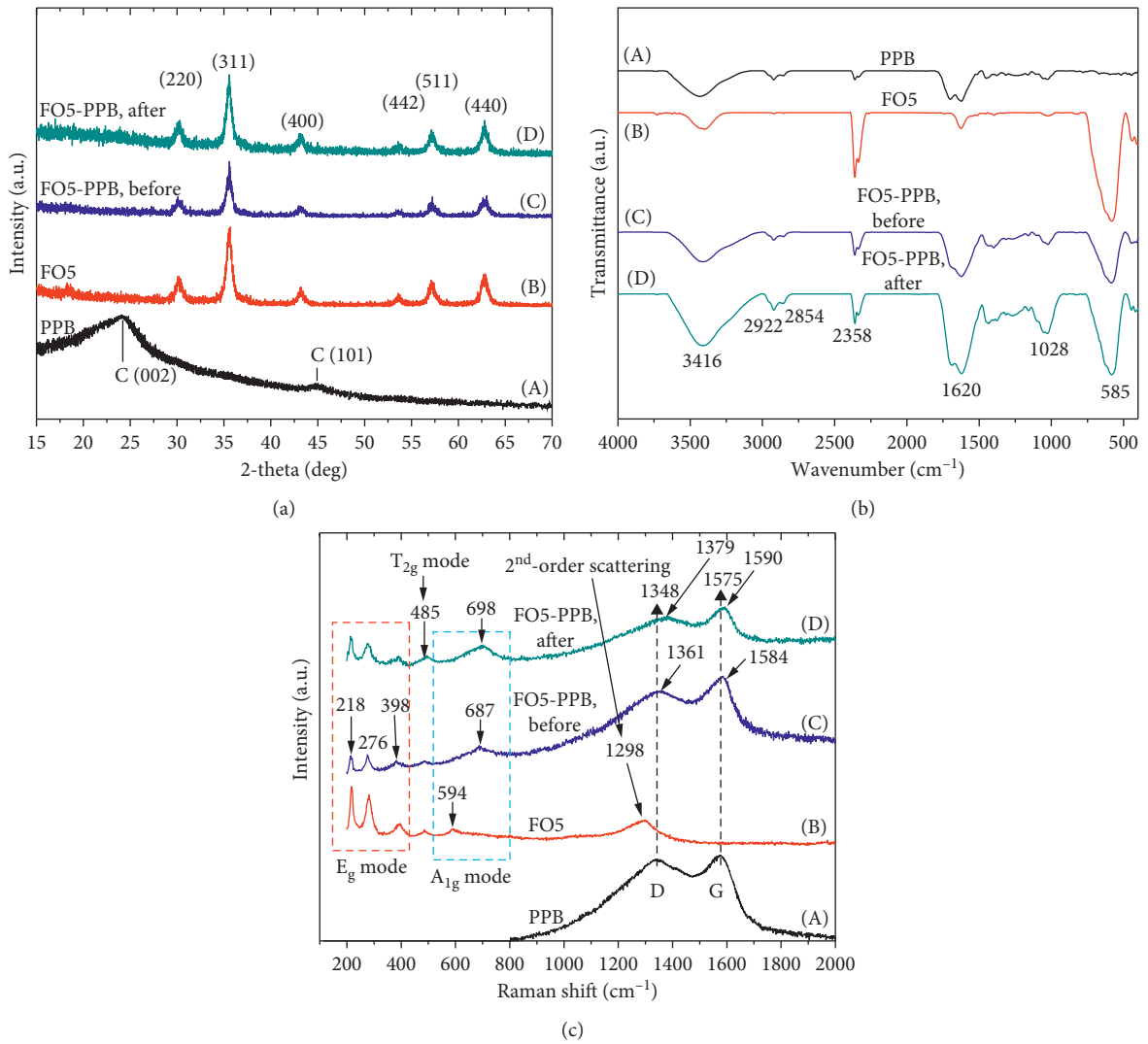

Figure 4: XRD patterns (a), FTIR spectra (b), and Raman spectra (c) of adsorbents.

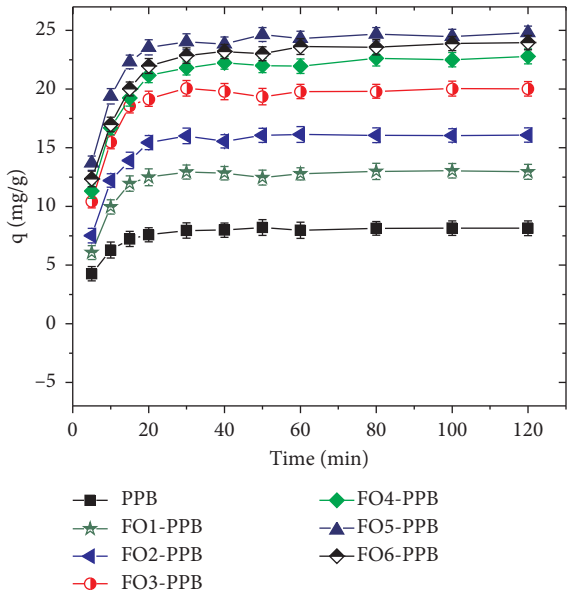

Figure 5: The effects of various impregnation ratios between Fe and PPB on the adsorption capacity of RR21. Conditional parameters: initial RP21 concentration: 50 mg/L; pH: 3; adsorbent dose: 2 g/L; temperature: 25 ± 2°C.

sharply while increasing solution pH from 3 to 11 (Figure 6(a)). The maximum adsorption capacity of RR21 by PPB and FO5-PPB reached 13.18 and 24.40 mg/g, respectively, at solution pH 3.0. The adsorption capacity of RR21 by FO5-PPB was also higher than that of pristine biochar (PPB). This was due to the successful composite of Fe_3O_4 onto PPB, leading to an increase in surface area, porosity, and heterogeneity of FO5-PPB compared to pristine PPB. The preference of Fe_3O_4 also enhances the adsorption capacity of R21 onto FO5-PPB.

In acidic conditions, the adsorbent has a positive charge while RR21, an anionic dye, has a negative charge. Therefore, their interaction could become more intensive in acidic conditions. This led to higher adsorption capacity at low pH. In a low pH, the electrostatic attraction between the positive charges on the surface of PPB and FO5-PPB with the sulfate groups (D-SO_3Na) in RP21 occurred. However, in a high pH, there was a competition for the adsorption sites between the hydroxide ions (OH^-) and anionic RR21. Therefore, the adsorption capacity of the adsorbent decreased when the solution pH was high, especially in alkaline conditions. Yang et al. [62] reported that if the equilibrium pH was lower than pH_{PZC}, electrostatic attraction would emerge between the negative charge of the anionic dye and the protonated hydroxide and carboxyl groups ($COOH^-$) on the surface of biochar.

From Figure 6(b), the pH_{PZC} values of PPB and FO5-PPB before adsorption were 5.6 and 8.2. These values increased to 6.4 and 9.1 after adsorption, respectively. When the solution pH was higher than pH_{PZC}, the electric charge on the surface of adsorbents turned negative and the electrostatic attraction would be weakened as a result. Hence, the RR21 adsorption capacity of PPB and FO5-PPB decreased with increasing solution pH. The pH_{PZC} of PPB and FO5-PPB increased after adsorption processes illustrated that anionic RR21 was successful to adsorb onto PPB and FO5-PPB.

Reactive dyes are anionic dyes due to the negative electrical structure of the chromophore group. When increasing the solution pH, the content of OH^- ions also increases. Consequently, it will compete with dye anions for biosorption sites. Therefore, there was a decrease in RR21 adsorption capacity as the solution pH increased. By contrast, the number of positively charged sites on the biosorbent surface available is higher at low pH values, leading to an enhancement of electrostatic attraction between negatively charged dye anions and adsorbents [63]. Therefore, solution pH of 3.0 was the best adsorption condition of RR21 by PPB and FO5-PPB, and this pH value was used for further experiments. The similar tendency was recorded in previous works. To be specific, Munagapati et al. [61] reported the decrease in Reactive Red 120 adsorption when the solution pH rose from 2 to 9. Aksakal et al. [63] also remarked that the adsorption capacity of Reactive Red 195 by the *Pinus sylvestris* Linnaeus adsorbent was declined corresponding to the increase in solution pH from 1 to 6.

3.2.3. Effect of Contact Time. The influences of contact time on adsorption capacity by PPB and FO5-PPB were studied with experimental conditions set at pH of 3, initial RR21 concentration of 50 mg/L, adsorbent dose of 2 g/L, and contact time lasting from 5 to 120 min. Figure 7 presents the results of RR21 adsorption capacity by PPB and FO5-PPB. The results showed that RR21 adsorption capacity increased significantly from 3.46 to 13.76 mg/g for PPB and from 10.73 to 23.90 mg/g for FO5-PPB while increasing the adsorption time from 5 to 50 min. However, the adsorption capacity almost remained constant when increasing the adsorption time from 60 min to 120 min. After 50 min of reaction, the maximum adsorption capacity of FO5-PPB reached 23.90 mg/g, much higher than that of PPB (10.73 mg/g). It can be due to a high number of vacant active sites on PPB and the FO5-PPB surface in the beginning stage. Therefore, the adsorption process occurred faster in the initial 30 minutes. However, the active sites of PPB and FO5-PPB decrease during the time of adsorption. Thus, the adsorption process increased slowly during the next contact periods. After 50 min of contact time, the active sites were almost fully occupied. It might be due to the adsorption and desorption processes that tend to be equal, leading to a decrease in the extent of adsorption. As a result, adsorption and desorption were at a balanced state, which led to a nearly constant equilibrium adsorption processes. This tendency was similar to many previous studies which investigated the adsorption of dyes from aqueous solutions by the *Pinus sylvestris* Linnaeus biosorbent [63] and biochar derived walnut shell and hazelnut shell [64]. Based on these results, the contact time of 50 min would be used for further experiments of RR21 adsorption.

3.2.4. Effect of Temperatures. Temperature is also an important factor that influences endothermic or exothermic process of adsorption. The effects of temperature on RR21 adsorption by PPB and FO5-PPB were examined by varying the temperature in a range of 20–40°C while keeping other parameters of needed experiments (solution pH of 3, initial concentration of 50 mg/L, contact time of 60 min, and adsorbent dose of 2 g/L). The results are illustrated in Figure 8. It is clear that the RR21 adsorption capacity by PPB and FO5-PPB increased from 12.05 mg/g to 15.42 mg/g and 22.12 mg/g to 26.20 mg/g, respectively, when increasing the solution temperature from 20°C to 40°C. This may be due to the increased porosity and the total pore volume of the adsorbent, leading to the higher number of available active sites on the adsorbent when the temperature rises [65, 66]. Simultaneously, the mobility of RR21 molecules also increases leading to a high potential of the interaction between RR21 and PPB and FO5-PPB. Furthermore, the high temperature could create a swell effect in the internal structure of activated carbon to allow more dye molecule diffusion into adsorbents [67]. The temperature increase resulted in an increase in the exchange rate between RR21 and functional groups available on the PPB and FO5-PPB surfaces. Therefore, the RR21 adsorption capacity was enhanced with the increase in solution temperature. These results indicate that RR21 adsorption onto PPB and FO5-PPB is an endothermic process. The similar tendency was also recorded in several studies [68].

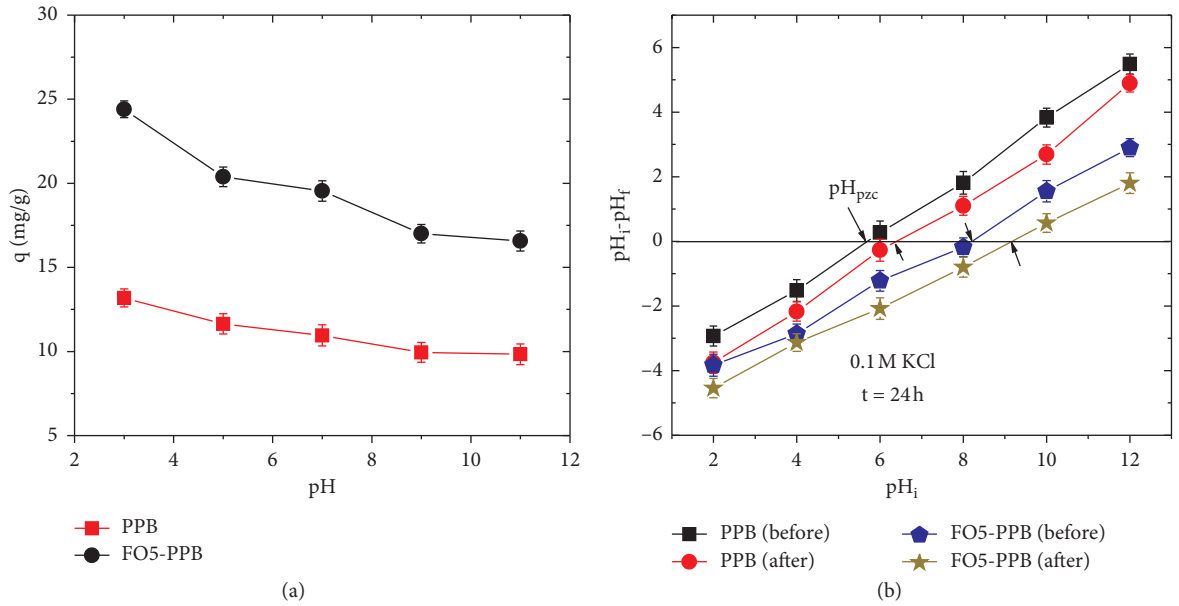

Figure 6: (a) The effects of pH on RR21 adsorption; (b) pH_{PZC} of PPB and FO5-PPB before and after adsorption. Conditional parameters: RP21 initial concentration: 50 mg/L; adsorbent dose: 2 g/L; adsorption time: 90 min; temperature: 25 ± 2°C.

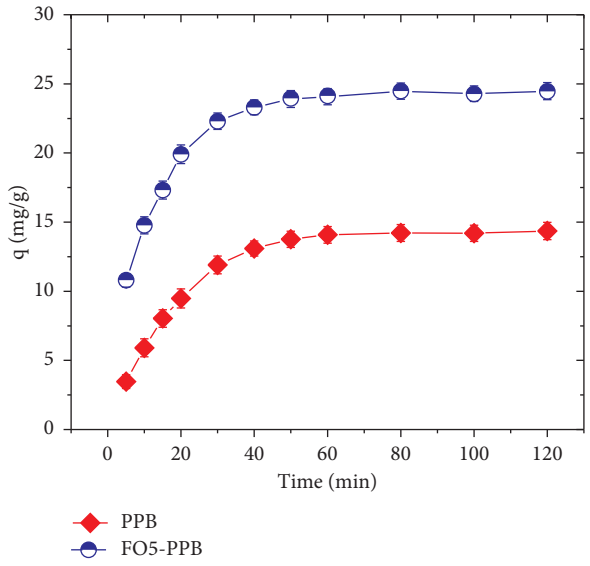

Figure 7: The effects of contact time on RR21 adsorption onto PPB and FO5-PPB. Experimental conditions: pH: 3; initial concentration: 50 mg/L; adsorbent dose: 2 g/L; temperature: 25 ± 2°C.

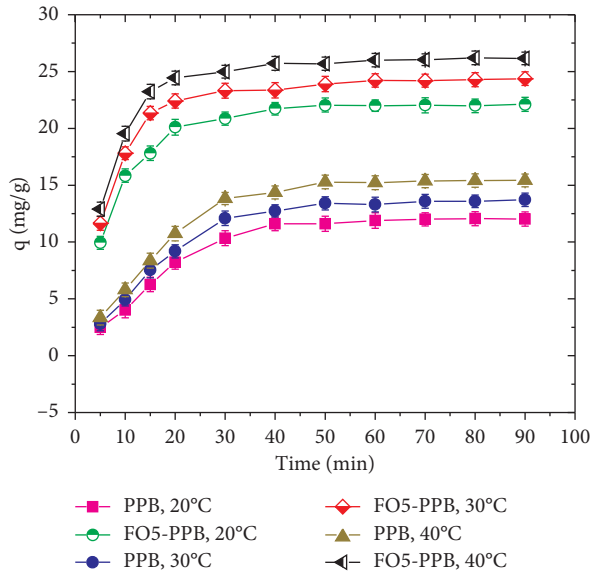

Figure 8: The effects of temperature on RR21 adsorption onto PPB and FO5-PPB. Experimental conditions: pH: 3; initial concentration: 50 mg/L; adsorbent dose: 2 g/L; contact time: 60 min.

3.2.5. Effect of Initial Concentration of Red 21. Initial RR21 concentration (varying from 50 to 800 mg/L), which is also a factor causing certain influences on the adsorption process by PPB and FO5-PPB, was also investigated. All experiments were conducted in 60 min of contact time and at solution pH 3, adsorbent dose of 2 g/L, and temperature of 40°C. Figure 9 presents the RR21 adsorption capacity onto PPB and FO5-PPB. The obtained results indicated that the adsorption capacity by PPB and FO5-PPB increased from 4.35 to 21.36 mg/g and 8.06 to 30.3 mg/g, respectively, at 40°C with the increasing initial RR21 concentrations from 50 to 300 mg/L. It can be explained that as the initial concentration increased, the driving force for the mass transfer between RR21 and PPB as well as FO5-PPB also increased which led to an enhancement of adsorption capacity. However, the adsorption capacity did not increase significantly when the initial RR21 concentration continuously increased to more than 300 mg/L. It was due to the limitation of the self-binding sites of adsorbents and the saturation of adsorption positions on the adsorbent surface. It can be explained that RR21 (dye anions) almost interacted with

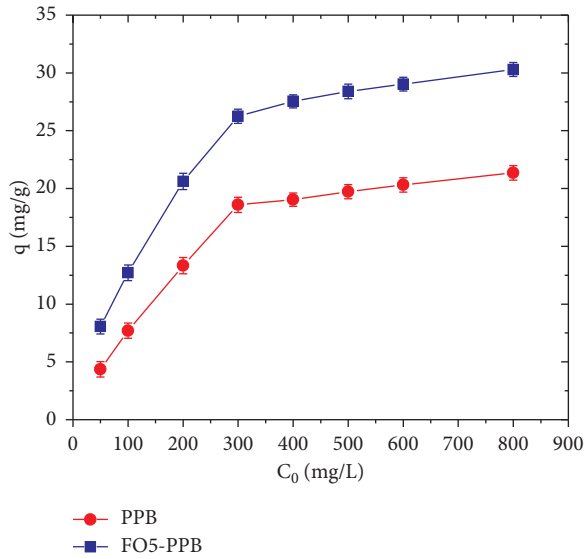

FIGURE 9: The effects of initial concentration on adsorption by PPB and FO5-PPB. Experimental conditions: pH: 3; adsorbent dose: 2 g/L; contact time: 60 min.

active sites on the PPB or FO5-PPB at a low initial RR21 concentration. By contrast, there was a decrease in active sites, leading to insufficient sites for dye anions to interact in case of a higher RR21 concentration. Results with resemblances have also been apprehended in other studies. Remarkably, Değermenci et al. reported that there was a decrease in the removal efficiency of Reactive blue 19 when there was an increase in the initial concentration of the employed contaminant [69].

3.2.6. Adsorption Isotherm. To study the equilibrium relationship between the adsorbent and the adsorbate, several common adsorption isotherm models were utilized to describe the RR21 adsorption processes onto PPB and FO5-PPB. Figure 10 presents a typical adsorption isothermal graph of q_e against C_e. The determination of the adsorption capacity of PPB and FO5-PPB was performed using the Langmuir (equation (3)) and Sips (equation (4)) isotherms. The respective parameters of those models are presented in Table 1:

$$q_e = \frac{Q^o_{\max} K_L C_e}{1 + K_L C_e}, \tag{3}$$

$$q_e = \frac{Q_m C_e^{n_s}}{b + C_e^{n_s}}, \tag{4}$$

where q_e and C_e are the results obtained from equation (1), $Q^o_{\max}$ (mg/g) is the maximum saturated adsorption capacity of the biosorbent, and K_L (L/mg) is the Langmuir constant related to the affinity between an adsorbent and an adsorbate; for the Sips model, q_e is denoted for the adsorbed amount at equilibrium (mg/g), C_e is the equilibrium concentration of the adsorbate (mg/L), Q_m is the denotation of the Sips maximum adsorption capacity (mg/g), K_S is the Sips equilibrium constant (L/mg), and n_S is for the Sips model exponent describing heterogeneity, with $b = (1/K_S)^{n_S}$. Figure 10 exhibits a typical isothermal graph of q_e against C_e regarding the adsorption process.

From Figure 10 and Table 1, it can be seen that Langmuir and Sips models were well appropriate for the adsorption data of RR21 onto PPB and FO5-PPB with high R^2 values that equal 0.9826 and 0.9854, respectively. The maximum adsorption capacity (q_m) of PPB and FO5-PPB calculated from the Langmuir model was approximately 17.23 and 26.82 mg/g, respectively. Meanwhile, the maximum calculated adsorption capacity (q_m) of PPB and FO5-PPB from the Sips model was 15.26 and 25.91 mg/g, respectively. These above calculated results were close to the experimental values (q_{mexp} of 14.36 and 24.47 mg/g for PPB and FO5-PPB, respectively). These results indicated that the RR21 adsorption process by PPB and FO5-PPB mainly occurs in monolayers or through a certain number of identical active sites on the surface of adsorbents [70]. In addition, all R_L values of the Langmuir model and other values of the Sips model were 0-1, showing that the adsorption of RR21 onto PPB and FO5-PPB is desirable. Similar reports were shown in some studies about reactive dye adsorption on magnetic adsorbents [21, 37].

3.2.7. Adsorption Kinetic of RR21 onto PPB and FO5-PPB. The pseudo-first-order (equation (5)) and pseudo-second-order (equation (6)) models were used to describe the kinetics of RR21 adsorption onto PPB and FO5-PPB:

$$q_t = q_e\left(1 - e^{-k_1 t}\right), \tag{5}$$

$$q_t = \frac{q_e^2 k_2 t}{1 + q_e k_2 t}, \tag{6}$$

where q_e and q_t are the adsorption capacity at equilibrium and at time t (mg/g); k_1 is the first-order rate constant (min^{-1}); k_2 is the second-order rate constant, g/mg. min; α is the initial adsorption rate (mg/g min); and β is the adsorption constant (g/mg) [71–76].

Figure 11 and Table 2 express the comparison of adsorption kinetic data for the pseudo-first-order and pseudo-second-order models. The calculated results show that the dynamics of RR21 adsorption onto PPB and FO5-PPB well fits both pseudo-first-order and pseudo-second-order models with high R^2 values (more than 0.95) at various solution temperatures from 20 to 40°C. The maximum calculated adsorption capacity (q_m) from the pseudo-first-order model was 18.72, 20.29, and 21.89 mg/g for PPB and 26.79, 29.18, and 30.39 mg/g for FO5-PPB at 20, 30, and 40°C, respectively (Table 2). The maximum adsorption capacity derived from the pseudo-second-order model was higher with 24.73, 26.64, and 28.41 mg/g for PPB and 33.98, 37.07, and 38.02 for FO5-PPB at 20, 30, and 40°C, respectively (Table 2). Both the pseudo-first-order and pseudo-second-order models are suitable to the obtained results from the experiments of this study. It suggests that valence forces through sharing or exchange of electrons between RR21 adsorption and PPB and FO5-PPB was the main

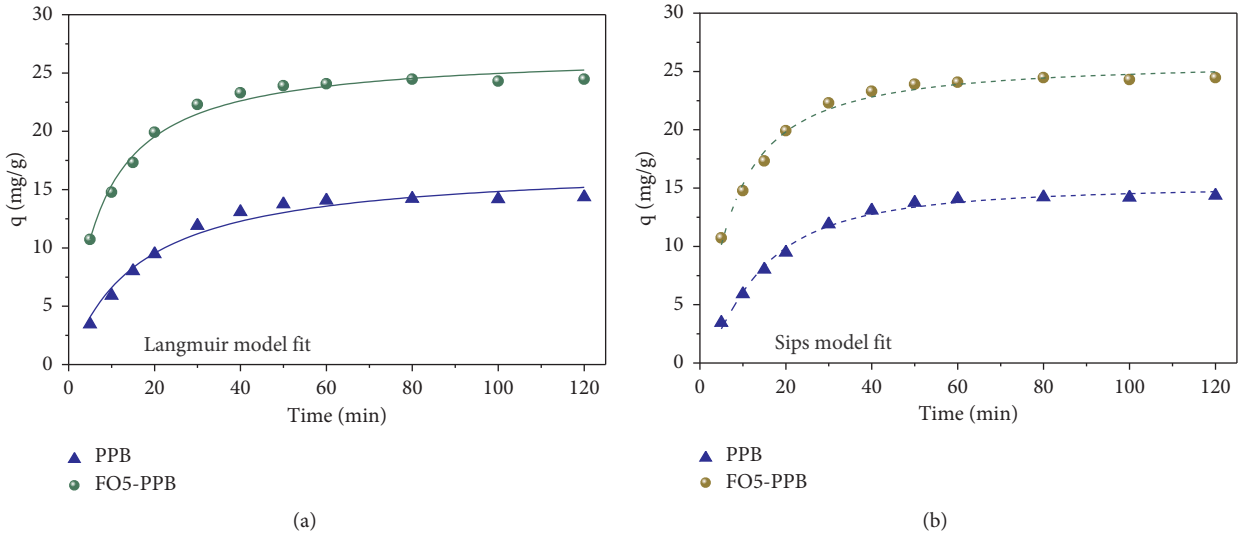

Figure 10: The adsorption isothermal equilibrium prediction of RR21 onto PPB and FO5-PPB at a contact time of 60 min and adsorbent dose of 2 g/L.

Table 1: Adsorption isothermal parameters and correlation coefficients of Langmuir and Sips models for RR21 adsorption onto PPB and FO5-PPB at different temperatures.

Model	Unit	PPB	FO5-PPB
Langmuir			
Q^o_{max}	mg/g	17.23	26.82
K_L	L/mg	0.062	0.134
R^2	—	0.9701	0.9826
Sips model			
Q^o_{max}	mg/g	15.26	25.91
b	—	0.022	0.097
n	—	0.679	0.854
R^2	—	0.9903	0.9854

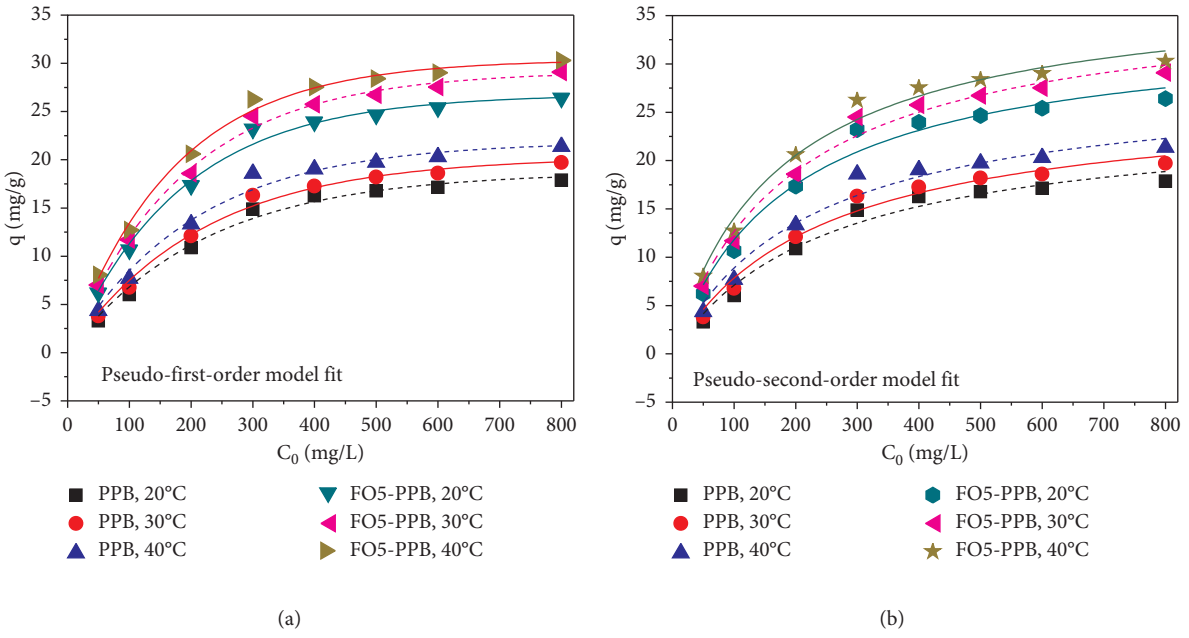

Figure 11: Adsorption kinetic prediction of RR21 onto PPB and FO5-PPB at a contact time of 60 min and adsorbent dose of 2 g/L at different temperatures.

Table 2: RR21 adsorption parameters of selective kinetic modes at different temperatures.

	Unit	Adsorbent					
		PPB 20°C	PPB 30°C	PPB 40°C	FO5-PPB 20°C	FO5-PPB 30°C	FO5-PPB 40°C
PFO model							
q_e	mg/g	18.72	20.29	21.89	26.79	29.18	30.39
k_1	g/mg × min	0.0045	0.0046	0.0049	0.0055	0.0053	0.0058
R^2	—	0.9865	0.9901	0.9830	0.9899	0.9938	0.9942
PSO model							
q_e	mg/g	24.73	26.64	28.41	33.98	37.07	38.02
k_2	1/min	$1.627.e^{-4}$	$1.564.e^{-4}$	$1.602.e^{-4}$	$1.567.e^{-4}$	$1.400.e^{-4}$	$1.544.e^{-4}$
R^2	—	0.9682	0.9754	0.9648	0.9721	0.9834	0.9799

mechanism [77]. This trend was similar with other reports of reactive dye adsorption onto biochar [31, 63]. They illustrated that reactive dye adsorption also fitted the pseudo-first-order and pseudo-second-order models.

4. Conclusion

In this study, the adsorption capacity of RR21 onto the Fe_3O_4-modified biochar derived from the pomelo peel was investigated. Pomelo peel biochar (PPB) and magnetic biochar composites from the pomelo peel with Fe_3O_4 (FO5-PPB) are positively capable of being an efficient adsorbent for eliminating RR21 from aqueous environments. This study has clarified that solution pH 3 was suitable for RR21 adsorption onto PPB and FO5-PPB. The maximum adsorption capacity of RR21 by PPB and FO5-PPB was 18.59 and 26.25 mg/g at 60 min of contact time, adsorbent dose of 2 g/L, solution temperature of 40 C, and initial RR21 concentration of 300 mg/L. Experimental results indicated that biochar-loaded Fe_3O_4 at a ratio of 5 : 1 (FO5-PPB) had a higher adsorption capacity for RR21 compared to the pristine biochar from the pomelo peel. Freundlich and Sips isotherm models and pseudo-first-order and pseudo-second-order kinetic models were used to describe the adsorption equilibrium data. The Langmuir and Sips models were the best models for the description of the adsorption isothermal equilibrium. In addition, experimental results show that kinetic data are fitted by the pseudo-first-order kinetic model with high correlation coefficients. The success of this study provides an effective method to remove organic contaminants from water based on the agricultural waste-derived adsorbent. Fe_3O_4-modified biochar from the pomelo peel is a promising material for the removal of reactive dyes from wastewater.

Data Availability

The data used to support the findings of this study are included within the article.

Conflicts of Interest

The authors declare no possible conflicts of interest.

Acknowledgments

This research was funded by the Ministry of Education and Training, Vietnam (B2019-TNA-15).

References

[1] M. Razali, J. F. Kim, M. Attfield et al., "Sustainable wastewater treatment and recycling in membrane manufacturing," *Green Chemistry*, vol. 17, no. 12, pp. 5196–5205, 2015.

[2] V. A. Oyanedel-Craver and J. A. Smith, "Sustainable colloidal-silver-impregnated ceramic filter for point-of-use water treatment," *Environmental Science & Technology*, vol. 42, no. 3, pp. 927–933, 2008.

[3] F.-Y. Yi, W. Zhu, S. Dang et al., "The development of a highly photostable and chemically stable zwitterionic near-infrared dye for imaging applications," *The Royal Society of Chemistry*, vol. 51, pp. 3989–3992, 2013.

[4] Y. Ji, C. Ma, J. Li et al., "A magnetic adsorbent for the removal of cationic dyes from wastewater," *Nanomaterials*, vol. 8, no. 9, pp. 710–713, 2018.

[5] N. Sivri and İ. Toroz, "Pollutants of textile industry wastewater and assessment of its discharge limits by water quality standards," *Nanomaterials*, vol. 7, no. 2, pp. 97–103, 2007.

[6] J. Saini, V. K. Garg, and R. K. Gupta, "Removal of Methylene Blue from aqueous solution by Fe3O4@Ag/SiO2 nanospheres: synthesis, characterization and adsorption performance," *Journal of Molecular Liquids*, vol. 250, pp. 413–422, 2018.

[7] A. A. Alqadami, M. Naushad, M. A. Abdalla, M. R. Khan, and Z. A. Alothman, "Adsorptive removal of toxic dye using Fe3O4-TSC nanocomposite: equilibrium, kinetic, and thermodynamic studies," *Journal of Chemical & Engineering Data*, vol. 61, no. 11, pp. 3806–3813, 2016.

[8] S. Mishra and A. Maiti, "Optimization of process parameters to enhance the bio-decolorization of reactive red 21 by *Pseudomonas aeruginosa* 23N1," *International Journal of Environmental Science and Technology*, vol. 16, no. 11, pp. 6685–6698, 2018.

[9] H. T. Van, T. M. P. Nguyen, V. T. Thao, X. H. Vu, T. V. Nguyen, and L. H. Nguyen, "Applying activated carbon derived from coconut shell loaded by silver nanoparticles to remove Methylene Blue in aqueous solution," *Water, Air, & Soil Pollution*, vol. 229, no. 12, pp. 393–406, 2018.

[10] H. A. Kiwaan, T. M. Atwee, E. A. Azab, and A. A. El-Bindary, "Photocatalytic degradation of organic dyes in the presence of nanostructured titanium dioxide," *Journal of Molecular Structure*, vol. 1200, p. 127115, 2020.

[11] A. A. El-Bindary, H. A. Kiwaan, A. F. Shoair, and A. R. Hawas, "A novel crosslinked amphoteric adsorbent thiourea formaldehyde calcium alginate: preparation, characterization and adsorption behaviors of removing color from acidic and basic dyes," *Desalination and Water Treatment*, vol. 151, pp. 145–160, 2019.

[12] A. Demirbas, "Agricultural based activated carbons for the removal of dyes from aqueous solutions: a review," *Journal of Hazardous Materials*, vol. 167, no. 1-3, pp. 1–9, 2009.

[13] B. H. Hameed, "Grass waste: a novel sorbent for the removal of basic dye from aqueous solution," *Journal of Hazardous Materials*, vol. 166, no. 1, pp. 233–238, 2009.

[14] M. A. M. Salleh, D. K. Mahmoud, W. A. W. A. Karim, and A. Idris, "Cationic and anionic dye adsorption by agricultural solid wastes: a comprehensive review," *Desalination*, vol. 280, no. 1-3, pp. 1–13, 2011.

[15] V. M. Vasconcelos, F. L. Ribeiro, F. L. Migliorini et al., "Electrochemical removal of reactive black 5 azo dye using non-commercial boron-doped diamond film anodes," *Electrochimica Acta*, vol. 178, pp. 484–493, 2015.

[16] H. T. Van, L. H. Nguyen, T. K. Hoang et al., "Using FeO-constituted iron slag wastes as heterogeneous catalyst for Fenton and ozonation processes to degrade reactive red 24 from aqueous solution," *Separation and Purification Technology*, vol. 224, pp. 431–442, 2019.

[17] J. Tie, Z. Zheng, G. Li et al., "Removal of an anionic azo dye direct black 19 from water using white mustard seed (semen sinapis) protein as a natural coagulant," *Journal of Water Reuse and Desalination*, vol. 9, no. 4, pp. 442–451, 2019.

[18] N. T. Hien, L. H. Nguyen, H. T. Van et al., "Heterogeneous catalyst ozonation of direct black 22 from aqueous solution in the presence of metal slags originating from industrial solid wastes," *Separation and Purification Technology*, vol. 233, pp. 115961–116011, 2020.

[19] N. C. Fernandes, L. B. Brito, G. G. Costa et al., "Removal of azo dye using fenton and fenton-like processes: evaluation of process factors by box-behnken design and ecotoxicity tests," *Chemico-Biological Interactions*, vol. 291, pp. 47–54, 2018.

[20] V. K. Gupta and Suhas, "Application of low-cost adsorbents for dye removal—a review," *Journal of Environmental Management*, vol. 90, no. 8, pp. 2313–2342, 2009.

[21] S. Joshi, V. K. Garg, N. Kataria, and K. Kadirvelu, "Applications of Fe3O4@AC nanoparticles for dye removal from simulated wastewater," *Chemosphere*, vol. 236, pp. 124280–124312, 2019.

[22] B. H. Hameed, "Spent tea leaves: a new non-conventional and low-cost adsorbent for removal of basic dye from aqueous solutions," *Journal of Hazardous Materials*, vol. 161, no. 2-3, pp. 753–759, 2009.

[23] X. H. Vu, L. H. Nguyen, H. T. Van et al., "Adsorption of Chromium (VI) onto Freshwater snail shell-derived biosorbent from aqueous solutions: equilibrium, kinetics, and thermodynamics," *Journal of Chemistry*, vol. 2019, Article ID 3038103, 11 pages, 2019.

[24] N. Kataria, V. K. Garg, M. Jain, and K. Kadirvelu, "Preparation, characterization and potential use of flower shaped Zinc oxide nanoparticles (ZON) for the adsorption of victoria blue B dye from aqueous solution," *Advanced Powder Technology*, vol. 27, no. 4, pp. 1180–1188, 2016.

[25] J. Saini, V. K. Garg, R. K. Gupta, and N. Kataria, "Removal of orange G and rhodamine B dyes from aqueous system using hydrothermally synthesized zinc oxide loaded activated carbon (ZnO-AC)," *Journal of Environmental Chemical Engineering*, vol. 5, no. 1, pp. 884–892, 2017.

[26] L. Ai, Y. Zhou, and J. Jiang, "Removal of methylene blue from aqueous solution by montmorillonite/$CoFe_2O_4$ composite with magnetic separation performance," *Desalination*, vol. 266, no. 1-3, pp. 72–77, 2011.

[27] V. Ranjithkumar, S. Sangeetha, and S. Vairam, "Synthesis of magnetic activated carbon/α-Fe_2O_3 nanocomposite and its application in the removal of acid yellow 17 dye from water," *Journal of Hazardous Materials*, vol. 273, pp. 127–135, 2014.

[28] Y. Wu, L. Cha, Y. Fan, P. Fang, Z. Ming, and H. Sha, "Activated biochar prepared by pomelo peel using H_3PO_4 for the adsorption of hexavalent chromium: performance and mechanism," *Water, Air, & Soil Pollution*, vol. 228, no. 10, pp. 1–9, 2017.

[29] B. Zhang, Y. Wu, and L. Cha, "Removal of methyl orange dye using activated biochar derived from pomelo peel wastes: performance, isotherm, and kinetic studies," *Journal of Dispersion Science and Technology*, vol. 41, no. 1, pp. 125–136, 2019.

[30] T. Zhao, Y. Yao, D. Li, F. Wu, C. Zhang, and B. Gao, "Facile low-temperature one-step synthesis of pomelo peel biochar under air atmosphere and its adsorption behaviors for Ag(I) and Pb(II)," *Science of the Total Environment*, vol. 640-641, pp. 73–79, 2018.

[31] D. Chen, S. Xie, C. Chen et al., "Activated biochar derived from pomelo peel as a high-capacity sorbent for removal of carbamazepine from aqueous solution," *RSC Advances*, vol. 7, no. 87, pp. 54969–54979, 2017.

[32] I. Pengsaket, K. Thamaphat, and P. Limsuwan, "Removal of Cu^{2+} from aqueous solutions by magnetic nanoparticles-pomelo peel composite," *Key Engineering Materials*, vol. 675–676, pp. 154–157, 2016.

[33] J. Zou, W. Chai, X. Liu, B. Li, X. Zhang, and T. Yin, "Magnetic pomelo peel as a new absorption material for oil-polluted water," *Desalination and Water Treatment*, vol. 57, no. 27, pp. 12536–12545, 2016.

[34] D.-X. Liu, J. Mu, Q. Yao et al., "Design of iron-ion-doped pomelo peel biochar composites towards removal of organic pollutants," *SN Applied Sciences*, vol. 1, no. 2, pp. 1–7, 2019.

[35] M. Pashai Gatabi, H. Milani Moghaddam, and M. Ghorbani, "Point of zero charge of maghemite decorated multiwalled carbon nanotubes fabricated by chemical precipitation method," *Journal of Molecular Liquids*, vol. 216, pp. 117–125, 2016.

[36] X. Ma, H. Yang, L. Yu, Y. Chen, and Y. Li, "Preparation, surface and pore structure of high surface area activated carbon fibers from Bamboo by steam activation," *Materials*, vol. 7, no. 6, pp. 4431–4441, 2014.

[37] A. Hamedi, F. Trotta, M. Borhani Zarandi et al., "In situ synthesis of MIL-100 (Fe) at the surface of Fe3O4@AC as highly efficient dye adsorbing nanocomposite," *International Journal of Molecular Sciences*, vol. 20, no. 22, pp. 5612–5620, 2019.

[38] S. Wang and G. Q. Lu, "Effects of oxide promoters on metal dispersion and metal–support interactions in Ni catalysts supported on activated carbon," *Industrial & Engineering Chemistry Research*, vol. 36, no. 12, pp. 5103–5109, 1997.

[39] G. Vaidyanathan, S. Sendhilnathan, and R. Arulmurugan, "Structural and magnetic properties of Co1–xZnxFe_2O_4 nanoparticles by co-precipitation method," *Journal of Magnetism and Magnetic Materials*, vol. 313, no. 2, pp. 293–299, 2007.

[40] B. Sutrisno, A. Hidayat, Z. Mufrodi et al., "Kajian Sifat dielektrik pada lempeng nanopartikel magnetit (Fe_3O_4) yang dienkapsulasi dengan polyvinyl alcohol (PVA)," *Journal of Nanotechnology*, vol. 19, no. 60, pp. 34–37, 2014.

[41] W. Wang, L. Zheng, F. Lu, R. Hong, M. Z. Q. Chen, and L. Zhuang, "Facile synthesis and characterization of magnetochromatic Fe3O4 nanoparticles," *AIP Advances*, vol. 7, no. 5, pp. 056317-056318, 2017.

[42] J.-P. Hu, R.-L. Liu, J.-S. Liu, S.-Y. Zhao, X. Lin, and W.-L. Lai, "Thermodynamic behavior of adsorption of copper (II) ion on

wuyi rock tea dreg," *Desalination and Water Treatment*, vol. 52, no. 37-39, pp. 7196–7204, 2014.

[43] R.-S. Juang, Y.-C. Yei, C.-S. Liao et al., "Synthesis of magnetic Fe 3 O 4/activated carbon nanocomposites with high surface area as recoverable adsorbents," *Journal of the Taiwan Institute of Chemical Engineers*, vol. 90, pp. 51–60, 2018.

[44] M. Jain, M. Yadav, T. Kohout, M. Lahtinen, V. K. Garg, and M. Sillanpää, "Development of iron oxide/activated carbon nanoparticle composite for the removal of Cr(VI), Cu(II) and Cd(II) ions from aqueous solution," *Water Resources and Industry*, vol. 20, pp. 54–74, 2018.

[45] S. A. Kahani, M. Hamadanian, and O. Vandadi, "Deposition of magnetite nanoparticles in activated carbons and preparation of magnetic activated carbons," in *Proceedings of the AIP Conference Proceedings*, vol. 929, pp. 183–188, Kashan, Iran, August 2007.

[46] B. Unal, Z. Durmus, H. Kavas, A. Baykal, and M. S. Toprak, "Synthesis, conductivity and dielectric characterization of salicylic acid-Fe_3O_4 nanocomposite," *Materials Chemistry and Physics*, vol. 123, no. 1, pp. 184–190, 2010.

[47] S. Zhang, H. Niu, Z. Hu, Y. Cai, and Y. Shi, "Preparation of carbon coated Fe_3O_4 nanoparticles and their application for solid-phase extraction of polycyclic aromatic hydrocarbons from environmental water samples," *Journal of Chromatography A*, vol. 1217, no. 29, pp. 4757–4764, 2010.

[48] K. Ren, W. Zhang, S. Cao, G. Wang, and Z. Zhou, "Carbon-based Fe_3O_4 nanocomposites derived from waste pomelo peels for magnetic solid-phase extraction of 11 triazole fungicides in fruit samples," *Nanomaterials*, vol. 8, no. 5, pp. 302–312, 2018.

[49] B. Lesiak, N. Rangam, P. Jiricek et al., "Surface study of Fe3O4 nanoparticles functionalized with biocompatible adsorbed molecules," *Frontiers in Chemistry*, vol. 7, pp. 1–16, 2019.

[50] M. Ghasemi, M. Zeinaly Khosroshahy, A. Bavand Abbasabadi, N. Ghasemi, H. Javadian, and M. Fattahi, "Microwave-assisted functionalization of Rosa Canina-L fruits activated carbon with tetraethylenepentamine and its adsorption behavior toward Ni(II) in aqueous solution: kinetic, equilibrium and thermodynamic studies," *Powder Technology*, vol. 274, pp. 362–371, 2015.

[51] Y. Wei, B. Han, X. Hu, Y. Lin, X. Wang, and X. Deng, "Synthesis of Fe_3O_4 nanoparticles and their magnetic properties," *Procedia Eng*, vol. 27, no. 2011, pp. 632–637, 2012.

[52] F. Tuinstra and J. L. Koenig, "Raman spectrum of graphite," *The Journal of Chemical Physics*, vol. 53, no. 3, pp. 1126–1130, 1970.

[53] A. C. Ferrari and J. Robertson, "Resonant Raman spectroscopy of disordered, amorphous, and diamondlike carbon," *Physical Review B*, vol. 64, no. 7, pp. 1–13, 2001.

[54] S. Reich and C. Thomsen, "Raman spectroscopy of graphite," *Philosophical Transactions of the Royal Society A: Mathematical, Physical and Engineering Sciences*, vol. 362, no. 1824, pp. 2271–2288, 2004.

[55] J. Dennison, M. Holtz, and G. Swain, "Raman spectroscopy of carbon materials," *Spectroscopy*, vol. 11, no. 8, pp. 38–45, 2008.

[56] E. Mitchell, F. De Souza, R. K. Gupta et al., "Probing on the hydrothermally synthesized iron oxide nanoparticles for ultra-capacitor applications," *Powder Technology*, vol. 272, pp. 295–299, 2015.

[57] E. Mitchell, R. K. Gupta, K. Mensah-Darkwa et al., "Facile synthesis and morphogenesis of superparamagnetic iron oxide nanoparticles for high-performance supercapacitor applications," *New Journal of Chemistry*, vol. 38, no. 9, pp. 4344–4350, 2014.

[58] S. Tiwari, D. M. Phase, and R. J. Choudhary, "Probing antiphase boundaries in Fe_3O_4 thin films using micro-Raman spectroscopy," *Applied Physics Letters*, vol. 93, no. 23, 2008.

[59] S. Tiwari, R. Prakash, R. J. Choudhary, and D. M. Phase, "Oriented growth of Fe_3O_4 thin film on crystalline and amorphous substrates by pulsed laser deposition," *Journal of Physics D: Applied Physics*, vol. 40, no. 16, pp. 4943–4947, 2007.

[60] A. M. Jubb and H. C. Allen, "Vibrational spectroscopic characterization of hematite, maghemite, and magnetite thin films produced by vapor deposition," *ACS Applied Materials & Interfaces*, vol. 2, no. 10, pp. 2804–2812, 2010.

[61] V. S. Munagapati, J.-C. Wen, C.-L. Pan, Y. Gutha, and J.-H. Wen, "Enhanced adsorption performance of reactive red 120 azo dye from aqueous solution using quaternary amine modified orange peel powder," *Journal of Molecular Liquids*, vol. 285, pp. 375–385, 2019.

[62] G. Yang, L. Wu, Q. Xian, F. Shen, J. Wu, and Y. Zhang, "Removal of congo red and methylene blue from aqueous solutions by vermicompost-derived biochars," *PLoS One*, vol. 11, no. 5, Article ID e0154562, 2016.

[63] O. Aksakal and H. Ucun, "Equilibrium, kinetic and thermodynamic studies of the biosorption of textile dye (Reactive Red 195) onto Pinus sylvestris L," *Journal of Hazardous Materials*, vol. 181, no. 1-3, pp. 666–672, 2010.

[64] N. Kaya, "A comprehensive study on adsorption behavior of some azo dyes from aqueous solution onto different adsorbents," *Water Science and Technology*, vol. 76, no. 2, pp. 478–489, 2017.

[65] H. Khoshsang, A. Ghaffarinejad, H. Kazemi, and S. Jabarian, "Synthesis of mesoporous Fe_3O_4 and Fe_3O_4/C nanocomposite for removal of hazardous dye from aqueous media," *Journal of Water and Environmental Nanotechnology*, vol. 3, no. 3, pp. 191–206, 2018.

[66] N. N. Nassar, "Rapid removal and recovery of Pb(II) from wastewater by magnetic nanoadsorbents," *Journal of Hazardous Materials*, vol. 184, no. 1-3, pp. 538–546, 2010.

[67] M. Ghasemi, S. Mashhadi, and J. Azimi-Amin, "Fe_3O_4/AC nanocomposite as a novel nano adsorbent for effective removal of cationic dye: process optimization based on Taguchi design method, kinetics, equilibrium and thermodynamics," *Journal of Water and Environmental Nanotechnolnogy*, vol. 3, no. 4, pp. 321–336, 2018.

[68] G. Annadurai, R.-S. Juang, and D.-J. Lee, "Adsorption of rhodamine 6G from aqueous solutions on activated carbon," *Journal of Environmental Science and Health, Part A*, vol. 36, no. 5, pp. 715–725, 2001.

[69] G. D. Değermenci, N. Değermenci, V. Ayvaoğlu, E. Durmaz, D. Çakır, and E. Akan, "Adsorption of reactive dyes on lignocellulosic waste; characterization, equilibrium, kinetic and thermodynamic studies," *Journal of Cleaner Production*, vol. 225, pp. 1220–1229, 2019.

[70] L. H. Nguyen, T. M. P. Nguyen, H. T. Van et al., "Treatment of hexavalent chromium contaminated wastewater using activated carbon derived from coconut shell loaded by silver nanoparticles: batch experiment," *Water, Air, & Soil Pollution*, vol. 230, no. 3, pp. 1–12, 2019.

[71] M. Yousefi, R. Nabizadeh, M. Alimohammadi, A. A. Mohammadi, and A. H. Mahvi, "Removal of phosphate from aqueous solutions using granular ferric hydroxide process optimization by response surface methodology," *Desalination and Water Treatment*, vol. 158, pp. 290–300, 2019.

[72] M. Yousefi, S. M. Arami, H. Takallo et al., "Modification of pumice with HCl and NaOH enhancing its fluoride

adsorption capacity: kinetic and isotherm studies," *Human and Ecological Risk Assessment: An International Journal*, vol. 25, no. 6, pp. 1508–1520, 2019.

[73] S. Mazloomi, M. Yousefi, H. Nourmoradi, and M. Shams, "Evaluation of phosphate removal from aqueous solution using metal organic framework; isotherm, kinetic and thermodynamic study," *Journal of Environmental Health Science and Engineering*, vol. 17, no. 1, pp. 209–218, 2019.

[74] M. Heydari Moghaddam, R. Nabizadeh, M. H. Dehghani, B. Akbarpour, A. Azari, and M. Yousefi, "Performance investigation of zeolitic imidazolate framework—8 (ZIF-8) in the removal of trichloroethylene from aqueous solutions," *Microchemical Journal*, vol. 150, no. 8, pp. 104185–104216, 2019.

[75] M. H. Dehghani, S. Tajik, A. Panahi et al., "Adsorptive removal of noxious cadmium from aqueous solutions using poly urea-formaldehyde: a novel polymer adsorbent," *MethodsX*, vol. 5, pp. 1148–1155, 2018.

[76] M. H. Dehghani, K. Yetilmezsoy, M. Salari, Z. Heidarinejad, M. Yousefi, and M. Sillanpää, "Adsorptive removal of cobalt(II) from aqueous solutions using multi-walled carbon nanotubes and γ-alumina as novel adsorbents: modelling and optimization based on response surface methodology and artificial neural network," *Journal of Molecular Liquids*, vol. 299, no. 1, pp. 112154–112214, 2020.

[77] K. Vikrant, K.-H. Kim, Y. S. Ok et al., "Engineered/designer biochar for the removal of phosphate in water and wastewater," *Science of The Total Environment*, vol. 616-617, pp. 1242–1260, 2018.